



Investigation of slip systems activity and grain boundary sliding in fine-grained superplastic zinc alloy

Wiktor Bednarczyk¹ · Jakub Kawałko² · Maria Wątroba³ · Michał Szuwarzyński² · Piotr Bała^{2,4}

Received: 7 June 2023 / Revised: 30 August 2023 / Accepted: 28 September 2023
© The Author(s) 2023

Abstract

Zn alloys are desirable candidates for biodegradable materials due to their great biocompatibility and sufficient mechanical properties. Nevertheless, the most popular strengthening method by grain refinement after cold processing is usually ineffective in Zn alloys. Besides highly anisotropic deformation through a dislocation slip, grain boundary sliding (GBS) plays an important role in total deformation in fine-grained Zn alloys at room temperature (RT). Herein, Zn–0.5Cu (wt. %) alloy is fabricated by RT equal channel angular pressing, and its deformation mechanisms in tension were systematically analyzed at strain rates from 10^{-4} s^{-1} to 10^0 s^{-1} . GBS contribution in total deformation was measured using surface markers and atomic force microscopy. In addition, dislocation slip activity was evaluated via electron-backscattered diffraction-based slip trace analysis. As a result, investigated alloy presents the GBS contribution in a total deformation at RT from 35% at the strain rate 10^0 s^{-1} to 70% at 10^{-4} s^{-1} . Simultaneously, the number of slip-deformed grains decreased from 97.5% to 8%. Moreover, the basal slip system was dominant at all strain rates, while the prismatic and the pyramidal $\langle c + a \rangle$ slip systems were activated at the higher strain rates. The results presented here for the first time clearly show the complexity of deformation mechanisms in fine-grained Zn–0.5Cu, at significantly different strain rate conditions.

Keywords Zinc alloys · Grain boundary sliding · Slip trace analysis · Slip activity · Strain rate

1 Introduction

Zinc alloys are a fast-growing material group dedicated to biodegradable implant applications. Recent scientific efforts focus primarily on the corrosion [1] and biological properties [2] of newly developed Zn alloys. Nevertheless, the mechanical behavior of Zn alloys remains not fully explored.

Numerous studies show the effect of mechanical processing on Zn alloys' strength and ductility. Most of them present an increase in ductility with a decrease in processing temperature and, therefore, a reduction in grain size. This phenomenon is common in Zn alloys and is revealed for different alloy-specific grain sizes. In Zn–3Ag–0.5 Mg alloy, grain size reduction from 1.8 μm to 1.2 μm increased ductility from ~ 50% to 120% [3]; while in Zn–0.4Mn–0.8Li alloy, ductility changes from ~ 38% to ~ 78% with average grain size reduction from 7.2 μm to 2.0 μm [4]. Excessive grain refinement, one of the most popular strengthening methods in metallic materials, may be ineffective in Zn alloys because it activates, not defined indisputably yet, mechanisms responsible for ductility increase in the expense of strength. Generally, grain boundary sliding (GBS) [5] and dynamic recrystallization (DRX) [6] are considered grain refinement softening driving forces.

GBS is one of the potential deformation mechanisms causing the grain refinement strengthening to become ineffective. Room-temperature (RT) GBS in Zn alloys has been intensively investigated for the Zn–Al system [7]. Nevertheless, only a few studies focused on the other

✉ Wiktor Bednarczyk
wiktor.bednarczyk@pw.edu.pl

¹ Faculty of Materials Science and Engineering, Warsaw University of Technology, Wołoska 141, 02-507 Warsaw, Poland

² Academic Centre for Materials and Nanotechnology, AGH University of Krakow, Al. A. Mickiewicza 30, 30-059 Krakow, Poland

³ Empa, Swiss Federal Laboratories for Materials Science and Technology, Laboratory of Mechanics of Materials and Nanostructures, Feuerwerkerstrasse 39, CH-3602 Thun, Switzerland

⁴ Faculty of Metals Engineering and Industrial Computer Science, GH University of Krakow, Al. A. Mickiewicza 30, 30-059 Krakow, Poland

biocompatible chemical compositions. Usually, a remarkable effect of GBS occurs in fine-grained Zn alloys with Cu or Ag additions, where the elongation to failure exceeds 400% at RT, e.g., 460% in Zn–1Cu [8], 510% in Zn–0.5Cu [5], and 660% in Zn–0.8Ag [9]. For example, superplastic flow in the cold-rolled fine-grained Zn–1Cu alloy was primarily attributed to a Zn/ZnCu₄ phase boundary sliding; however, no additional GBS analyses were provided in this field [8]. In Zn–4Ag–0.6Mn alloy, with a grain size below 1.2 μm , the dominant deformation mechanism changes from dislocation slip to phase boundary sliding type of GBS [10]. More complex deformation studies were made on Zn–Li alloys, where GBS tends to be an important component of observed creep behavior [11].

The GBS phenomenon has been widely investigated for fine-grained materials at high-temperature. Assuming GBS as a creep deformation mechanism, it could be described through a general power-law relationship:

$$\dot{\epsilon} = \frac{ADGb}{kT} \left(\frac{b}{d}\right)^p \left(\frac{\sigma}{G}\right)^{1/m}, \quad (1)$$

where A is a dimensionless constant, D is the diffusion coefficient, G is the shear modulus, b is the Burgers vector, k is the Boltzmann's constant, T is the absolute temperature, d is the grain size, σ is the applied stress, p is the grain size exponent, and m is the stress rate sensitivity parameter ($m \approx 0.5$ for GBS) [12]. Considering phenomena occurring in Zn alloys, temperature, grain refinement, and strain rate are key factors that affect the main deformation mechanisms. Therefore, it can be easily investigated under constant two of the three mentioned variables.

Besides a high contribution of GBS in total deformation in Zn alloys, slip systems activity remains an important factor determining mechanical properties and deformation behavior in all metallic materials. Zn crystallizes in a hexagonal close-packed (HCP) highly anisotropic structure with a c/a ratio equal to 1.856 [13]. It significantly affects the stress required to activate available dislocation deformation modes in Zn. The ratio between basal $\langle a \rangle$, prismatic $\langle a \rangle$, pyramidal $\langle c + a \rangle$, and twinning systems is determined as: 1:15:10:30, respectively [14]. The basal slip system is expected to dominate in the deformation of Zn and its alloys. However, the presented ratio is valid for hot-processed coarse-grained Zn, while grain refinement significantly changes the deformation behavior. Grain refinement below a critical value in Zn suppresses twinning and changes the dominant deformation mode from twinning to dislocation slip. This phenomenon was observed in Zn and its alloys with grains size below a few μm [5] and precisely described for Mg [15]. Thus, twinning is not expected to occur in fine-grained Zn alloys.

The precise evaluation of dislocation slip activity is challenging not only in Zn but in any material. Usually, numerical crystal plasticity models are utilized to calculate the relative contribution of each slip system [16, 17]. Unfortunately, for Zn alloys, GBS is not considered in these models; thus, the results may be accurate for coarse-grained Zn alloys but not fine-grained ones. An electron-backscattered diffraction-based (EBSD) slip trace analysis is one of the imaging-based methods used to directly measure the relative activity of particular slip systems in a deformed sample. This method was successfully applied to HCP metals, e.g., Ti [18] and Mg alloys [19], making it suitable for Zn alloys. Additionally, slip trace analysis allows measuring dislocation slip deformation effects at any chosen deformation point using both in- and ex situ deformation methods.

The present article describes, for the first time, the activity of GBS and particular slip systems in the fine-grained Zn–0.5Cu (wt.%) alloy. The investigation was undertaken with two main objectives. First, to measure the GBS contribution in the total deformation at a wide range of strain rates. Second, to determine the effect of strain rate on slip systems activity during tension. Additionally, the present work utilizes a slip trace analysis to investigate deformation in the Zn–0.5Cu alloy, which has never been done so far for Zn alloys.

2 Materials and methods

The material used for the research was Zn–0.5Cu (wt.%) alloy processed by RT equal channel angular pressing (ECAP) to obtain fine-grained, equiaxed, fully recrystallized microstructure [20]. The alloy was prepared by induction melting at 650 $^{\circ}\text{C}$, casting into a steel mold, and subsequently annealing at 400 $^{\circ}\text{C}$ for 4 h, followed by water quenching. ECAP process was performed four times at RT using route B_C (rotation by 90 $^{\circ}$ after each pass) through a square cross-section channel with an angle equal to 90 $^{\circ}$. Additionally, molybdenum disulfide lubricant was used to reduce friction between sample and channel. Flat dog-bone double-narrowed samples with a gauge length of 3 mm and cross-section of 2 \times 1.5 mm [21] for mechanical and microstructural studies were cut using a wire-EDM machine (Mitsubishi FA10S) along the ECAP extrusion direction. The channel geometry and sample orientation are presented in Fig. 1. Specific sample geometry reduces the deformation area, simplifying SEM observation. Then, samples were carefully ground, polished with water-free suspensions, and Ar⁺ ion-polished (Hitachi IM4000 ion milling system) to remove the deformed layer. Further, a shallow grid with 5 μm spacing and tensile markers was etched on the investigated surface using a focused ion beam (FIB) installed in an FEI Quanta 3D 200i scanning electron microscope (SEM).

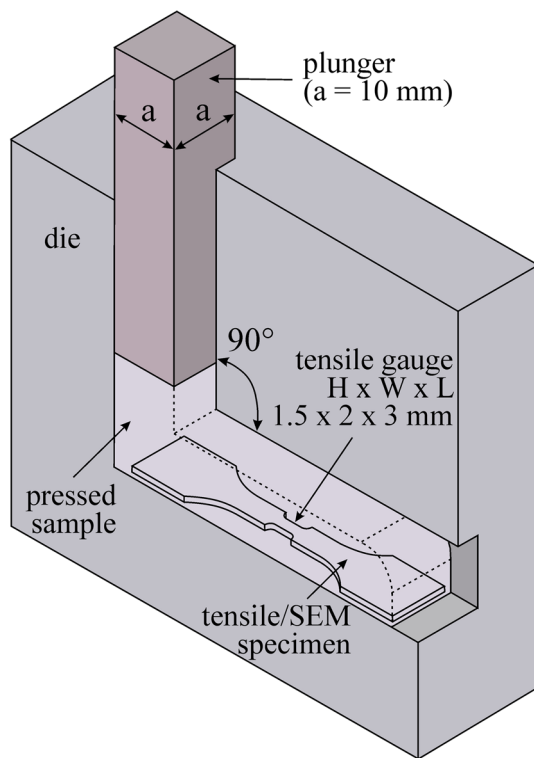


Fig. 1 Schematic representation of ECAP process and testing samples orientation

Tensile tests interrupted at ~25%, and ~50% of elongation were performed at RT, at strain rates from 10^{-4} s^{-1} to 10^0 s^{-1} using a 5 kN Kammrath & Weiss in situ tensile stage in an FEI Versa 3D SEM. Absolute deformation values were calculated post-mortem based on the relative displacement of FIB markers on the gauge section. Atomic force microscope (AFM) topography images were obtained with Bruker Dimension Icon XR microscope working in the air in the PeakForce Tapping mode using standard silicon cantilevers of the nominal spring constant of 0.4 N/m and triangular geometry tip with a nominal tip radius of 2 nm. Additionally, EBSD scans were performed at 20 kV with a 60 nm step size using an Oxford Symmetry S2 EBSD detector installed in FEI Versa 3D SEM.

Grain boundary sliding contribution ξ in the total deformation was determined directly from the following relationship [7]:

$$\xi = \frac{\varepsilon_{GBS}}{\varepsilon}, \quad (2)$$

$$\varepsilon_{GBS} = \phi \frac{(u, v, w)}{\bar{L}}, \quad (3)$$

where ϕ is an empiric factor equal to 1 for u measurements, otherwise 1.5, u , v , and w are mean values of

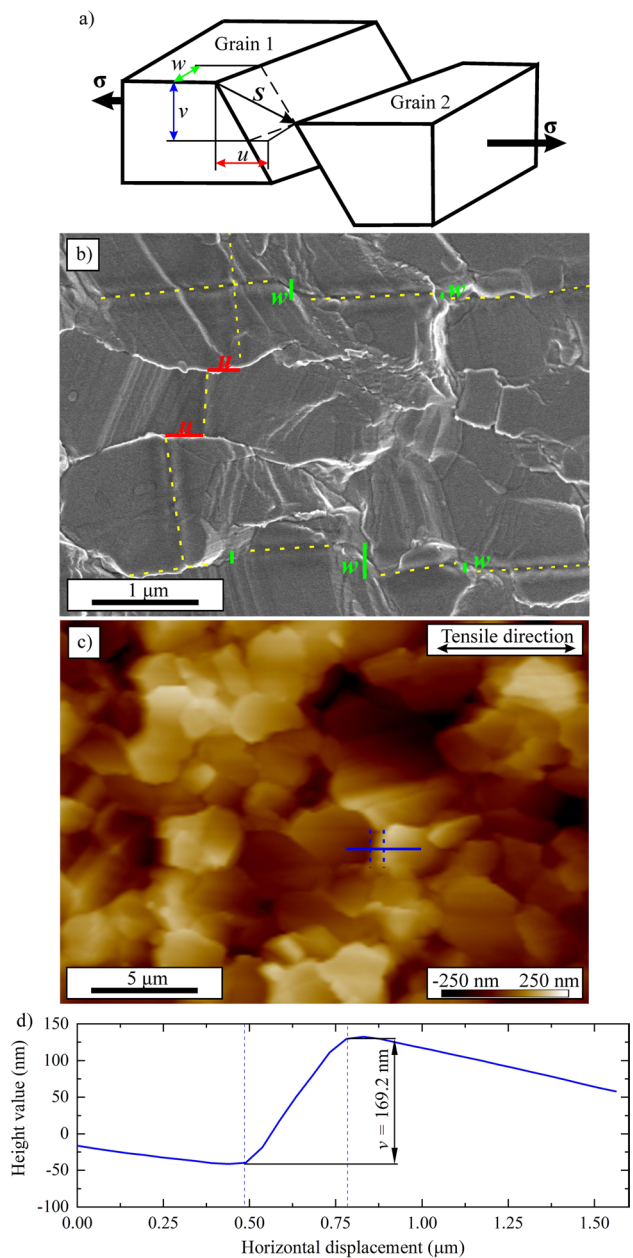


Fig. 2 **a** Schematic representation of grain boundary sliding, an example of **b** in-plane measurements of grain boundary displacement using SEM imaging of surface markers ($\dot{\varepsilon} = 10^{-2} \text{ s}^{-1}$), **c** out-of-plane measurements of grain boundary displacement using ex situ AFM-based measurements ($\dot{\varepsilon} = 10^{-4} \text{ s}^{-1}$), **d** the profile of single grain boundary displacement marked in image (c)

measured grain boundary displacement as presented in Fig. 2a, while \bar{L} is an arithmetic mean grain size (GS_0) obtained from the EBSD analysis. Preliminary analyses of u and w displacements were performed at strain rates 10^{-2} s^{-1} and 10^{-4} s^{-1} using surface markers (Fig. 2b). Nevertheless, relatively low precision of measurements compared to the grain size and low statistics disallow correct determination of ξ . Therefore, the major part of the investigation utilizes a

measurement of out-of-plane grain boundary v displacement by AFM mapping (Fig. 2c, d).

Figure 3 presents an example of slip trace analysis of samples deformed at strain rates equal 10^{-4} s^{-1} (Fig. 3a–c), and 10^{-1} s^{-1} (Fig. 3d–f) performed in $\{0001\}\langle 11\bar{2}0 \rangle$ basal, $\{10\bar{1}0\}\langle 11\bar{2}0 \rangle$ prismatic, and $\{11\bar{2}2\}\langle 11\bar{2}3 \rangle$ pyramidal slip systems based on the EBSD measurements using MTEX Toolbox in MATLAB [22, 23]. The twinning activity has not been analyzed because it was not observed in Zn–0.5Cu alloy with a grain size of $\sim 2.0 \mu\text{m}$ in wide strain rates [5]. Furthermore, during EBSD analysis, twins were not detected. The multi-step EBSD data analysis consisted of grain reconstruction and identification, average grain orientation calculation, and determination of slip trace with the highest Schmid factor in each considered slip system family for every identified grain. In the final step, maps of geometrically favored slip traces were plotted and superimposed on high-resolution SEM images to compare the calculated and detected slip traces.

3 Results

Figure 4 presents the microstructure at 25% tensile elongation at a wide range of strain rates. Samples strained at 10^0 s^{-1} were not tested up to 50% due to visible cracks. All

grains are severely deformed at the highest strain rate, and few intra-granular cracks occur. At strain rates in the range $10^0 \div 10^{-2} \text{ s}^{-1}$ (Fig. 4a–c), sharp slip traces can be seen; however, the grain boundary sliding also occurs. Decreasing strain rate increases the minimal size of grains deformed through slip, which implies an increasing grain boundary sliding activity at the expense of slip deformation. Therefore, only the biggest grains reveal evident slip traces at a strain rate equal to or lower than 10^{-3} s^{-1} (Fig. 4d,e). Besides the surface topography analysis, the average grain size was calculated for each investigated sample and presented in Fig. 4.

The observed microstructure corresponds well with the tensile curves (Fig. 5a) measured during the tensile deformation. Curves registered at the two highest strain rates present significant strain softening. Additionally, the shallow second stress peak at the strain rate 10^0 s^{-1} most probably results from the occurrence of continuous dynamic recrystallization. Straining at a strain rate equal to or lower than 10^{-2} s^{-1} does not cause visible strain softening up to 50%. Applied different strain rates result in changes in deformation curves which reflect on flow stress values variations presented in Fig. 5b. The high-stress deformation at higher strain rates is realized through dislocation slip with low strain rate sensitivity parameter $m=0.04$, while the reduction in the strain rate reduces flow stress and increases strain rate sensitivity

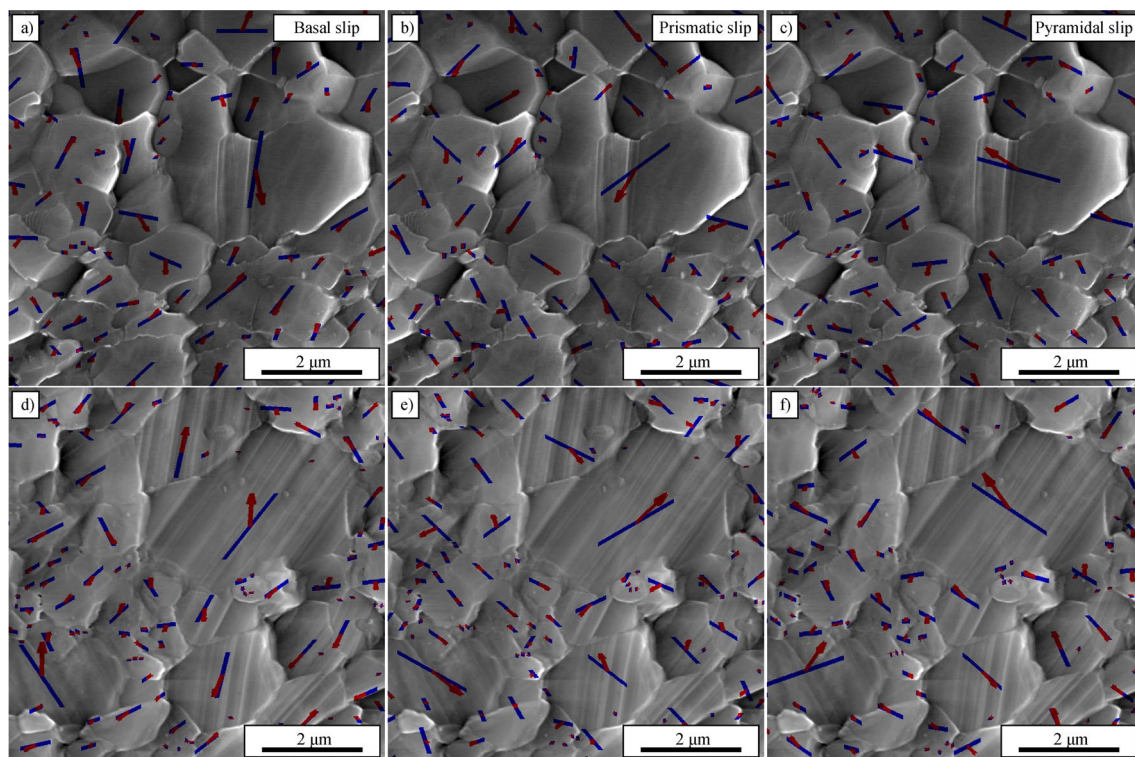


Fig. 3 EBSD-based slip trace analysis in **a,d** basal $\langle a \rangle$, **b,e** prismatic $\langle a \rangle$, and **c,f** pyramidal $\langle c+a \rangle$ slip systems after the deformation to 25% at the strain rate of **a–c** 10^{-4} s^{-1} , **d–f** 10^{-1} s^{-1}

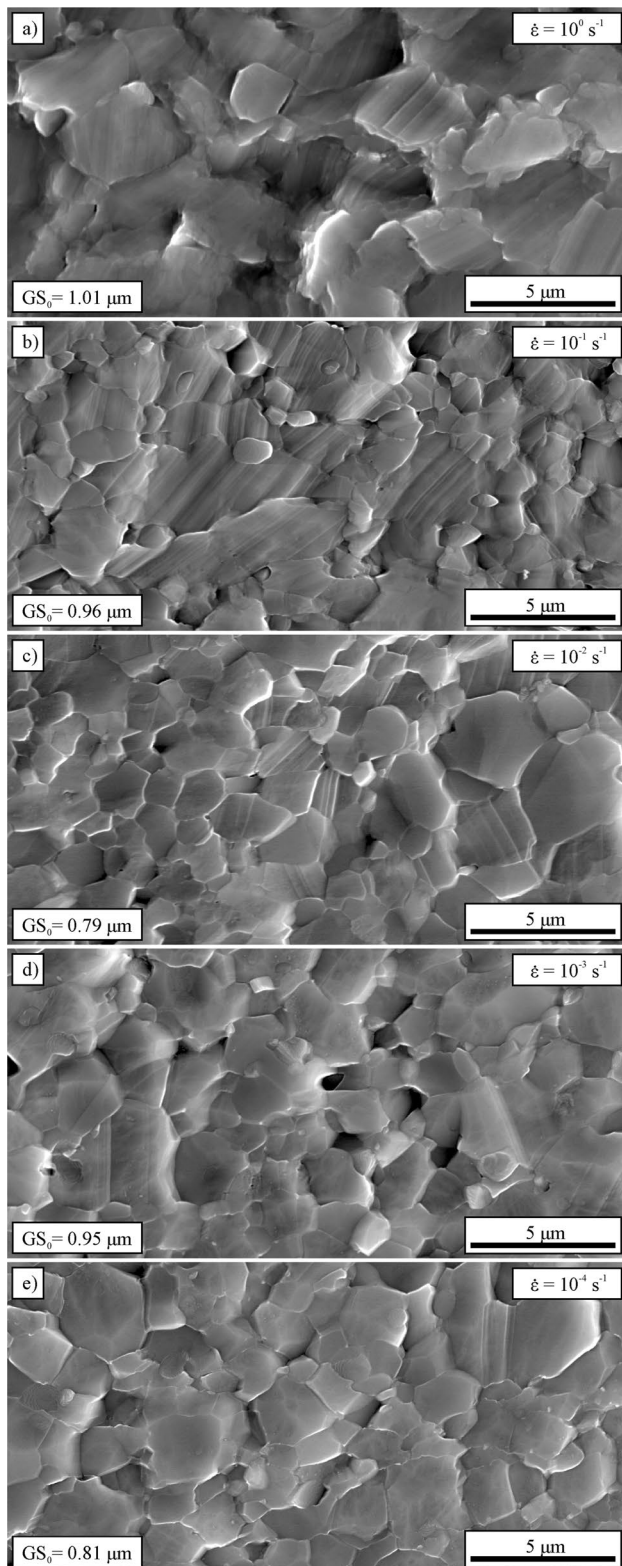


Fig. 4 SEM surface images after the deformation to 25% at strain rate: **a** 10^0 s^{-1} , **b** 10^{-1} s^{-1} , **c** 10^{-2} s^{-1} , **d** 10^{-3} s^{-1} , **e** 10^{-4} s^{-1}

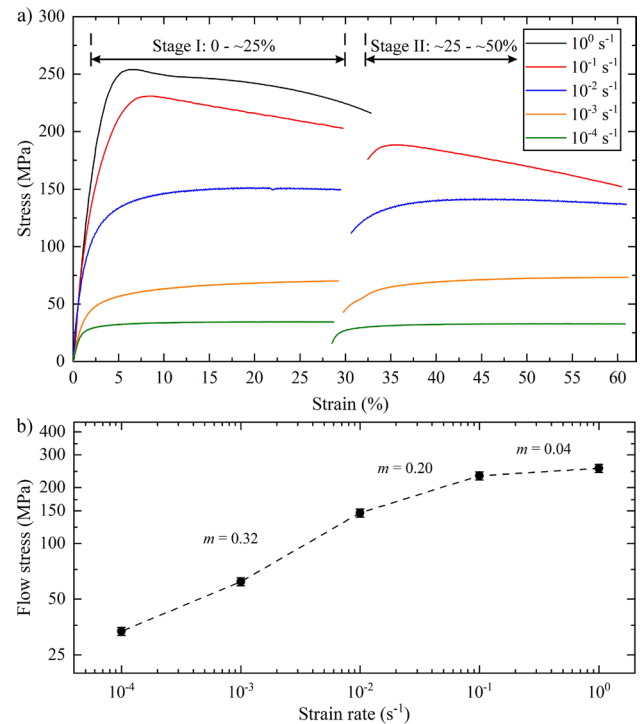
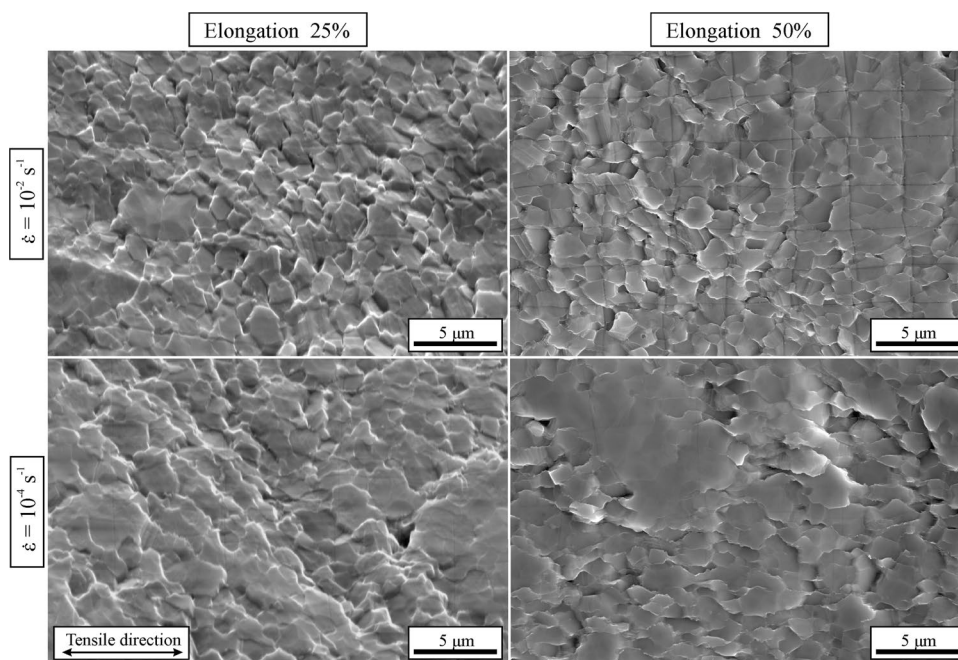


Fig. 5 **a** Tensile engineering stress–strain curves corresponding to the investigated Zn-0.5Cu alloy at various initial strain rates, **b** variation of flow stress at 7.5% with strain rate at RT

to $m = 0.32$. This implies a high contribution of GBS in total deformation and low dislocation slip activity at low strain rates. The measured strain rate sensitivity parameter m agrees with previously reported values [5, 20].

The deformation modes activity in fine-grained Zn–0.5Cu alloys has been investigated in two steps. First, the measurements of GBS contribution ξ to total deformation, and second, slip trace analysis of three possible slip systems. SEM images and AFM maps collected for GBS analysis are presented in Figs. 6 and 7, respectively, while Fig. 8a presents the summary of quantitative ξ results in a wide range of strain rates. The direct comparison of GBS determination methods shows significant discrepancies between in-plane u and w marker-based measurements. ξ values calculated for GB displacement u parallel to the tensile direction are 20% higher than values obtained for perpendicular in-plane displacement w . The additional amount of GBS may result from the dislocation-based (either slip or creep) deformation of grains between two marker parts visible in Fig. 2b. Much better agreement in ξ is observed between out-of-plane v and in-plane w measurements. Furthermore, the AFM-based measurements of ξ at 25% and 50% of elongation present the same tendency regardless of applied strain, implying steady deformation behavior at a wide range of strains. GBS is responsible for 70% of total deformation at strain rate 10^{-4} s^{-1} . Surprisingly, an increase in strain rate does not

Fig. 6 SEM images of deformed GBS markers at strain rates equal 10^{-2} s^{-1} and 10^{-4} s^{-1} . Vertical and horizontal lines were utilized to measure u and w displacements, respectively. (Measurements were taken from the higher magnification images)



reduce ξ continuously. It stabilizes at 45% for intermediate strain rate values and decreases to $\sim 40\%$ at 10^{-1} s^{-1} . Even at the highest strain rate equal 10^0 s^{-1} , GBS plays a meaningful role in a total deformation causing approx. 35% of the total deformation of samples strained to 25%.

Since GBS contributes to only a part of the total deformation, the dislocation slip has to be analyzed to obtain comprehensive information on deformation behavior in the fine-grained Zn–0.5Cu alloy. Figure 9 presents EBSD maps used for slip trace analysis after the deformation to 30%. EBSD measurements were not possible for higher deformation due to significant relief and its shading. Figure 8b presents the fraction of grains identified as deformed in a particular slip system or undeformed to a total number of grains after the deformation to 25%. An analysis for a higher deformation was impossible due to a significant surface relief. Initially, all grains identified as undeformed were counted and removed from further analysis. A fraction of deformed grains strongly depends on an applied strain rate; however, the measured tendency is linear in contrast to the double sigmoidal-like GBS activity curve. More than 97.5% of grains are deformed at the strain rate 10^0 s^{-1} , while at the lowest strain rate 10^{-4} s^{-1} , only 8% of grain exhibits visible slip traces. It is essential to mention that presented herein and after values relate to the total number of observed grains, not to a strain accommodated by a particular slip system. In Fig. 8b, a remarkable effect of strain rate on detected basal slip traces can be seen. Tension at the lowest strain rate induces deformation in the basal slip system only in a few biggest grains. An increase in strain rate significantly increases the grain fraction with visible basal slip traces

up to $\sim 82\%$. Investigation of prismatic and pyramidal slip systems turned out to be much more challenging. Besides the highest strain rate, the number of grains identified as deformed through prismatic or pyramidal slip systems was low, and its value oscillates at about 3%. At the highest strain rate, the activity of both mentioned above non-basal slip systems raised to approx. 7%. Nevertheless, non-basal slip systems activity analysis may give underestimated values due to its shallow slip traces and a prevailing effect of basal slip, weakening traces of other slip systems.

4 Discussion

The estimation of GBS contribution in total deformation is usually performed using various methodologies. ξ in coarse-grained materials deformed at an elevated temperature is commonly quantified based on the displacement of intrinsic or extrinsic markers. Errors in markers preparation and displacement measurements are relatively low compared to the grain size; thus, the relative error is acceptable. In fine-grained materials, the situation becomes more challenging. As presented here, the thickness of the FIB-marked grid to relative grains displacement ratio is quite high, while the resolution of imaging could not be enhanced significantly. Additionally, visible slip traces indicate the multicomponent phenomena of markers movement. Thus, significant differences between results obtained in in-plane longitudinal u and transversal w directions occurred in this study, indicating the need to discard one of these methods. In addition, out-of-plane displacement v measurement allows us to investigate ξ

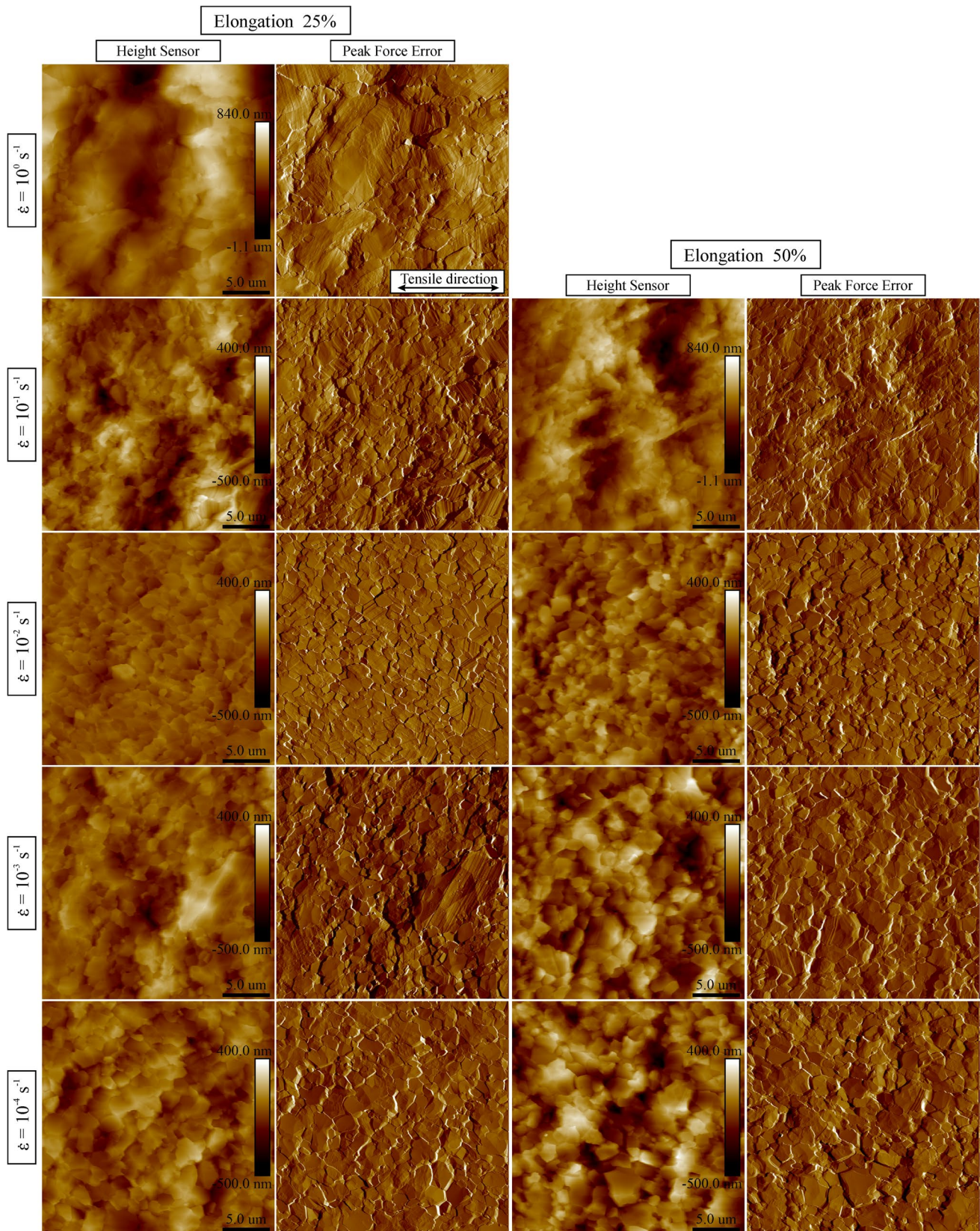


Fig. 7 AFM maps of deformed Zn-0.5Cu samples at strain rate from 10^{-4} s^{-1} to 10^0 s^{-1} . *Height Sensor* maps represent true height changes on the surface, while *Peak Force Error* maps present changes in the probe-taping parameters illustrating local changes on the surface

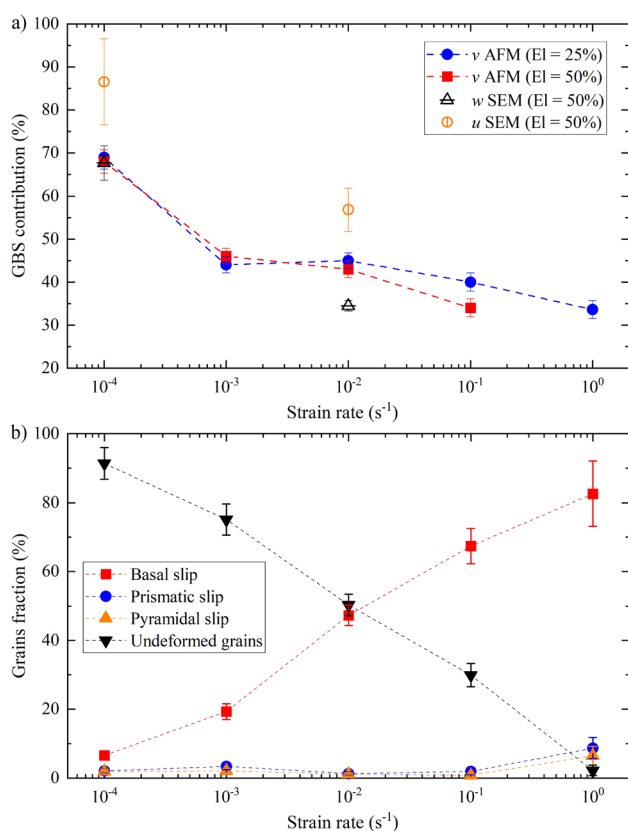


Fig. 8 The effect of strain rate on **a** GBS activity measured in three perpendicular directions, **b** a fraction of grains with an identified specific slip trace after the deformation to 25%

even in challenging fine-grained materials. Often used AFM detects even the most minor vertical displacement v , significantly enhancing measurement precision and omitting the slip trace effects. Summarizing, the results presented here show a better agreement between measurements in the w and v directions and considerably overestimated values in the u direction (due to slip). It correlates well with the comprehensive early research, which recommends both w and v directions in ξ analysis [24].

A high contribution of GBS in fine-grained single-phase Zn–0.5Cu alloy was presumed based on high-strain rate sensitivity parameter $m=0.31$ and elongation to failure above 400% [25]. The results presented here indicate a high ξ in Zn–0.5Cu alloy at a wide range of strain rates. The ξ value of 70% obtained in this research agrees with the results of other superplastic materials tested in GBS-dominant conditions [7, 26]. The missing 30% of strain is concealed in dislocation accommodation. Even at intermediate strain rates, a high ξ indicates a superplastic flow-dominant deformation in the investigated alloy with an increasing effect of dislocation slip while the strain rate increases. Many studies reported in the literature try to explain the high elongation and strain rate sensitivity in various fine-grained Zn alloys. GBS is

assumed as the key factor affecting mechanical properties in ultrafine-grained materials [5], while slip-induced dynamic recrystallization is supposed to dominate in Zn alloys with coarse and slightly refined microstructure, e.g., in Zn–Cu alloys [6], Zn–0.2 Mg alloy [27], and Zn–3Ag–0.5 Mg alloy [28]. Such a strict division stands in contrast with the results presented here, where both slip and GBS coincide in the fine-grained Zn alloy at a wide range of strain rates. Moreover, a limited GBS activity during indentation measurements was observed in huge-grained pure Zn, confirming its presence even in coarse-grained microstructure [29]. Zn and its alloys exhibit GBS at RT, which equals 0.43 of its absolute melting temperature. Thus, it could be assumed as an ambient-temperature creep mechanism. Nevertheless, creep tests performed on pure Zn with various grain sizes revealed the activation energy of GBS at the value of only one-sixth of the grain boundary diffusion. Therefore, GBS could be activated by short atomic rearrangement, e.g., absorption of piled-up dislocations by grain boundaries named slip-induced GBS [30].

Deformation through dislocation slip is an important mechanism in Zn alloys, even when the GBS plays a significant role. However, the relative activity of individual slip systems has never been investigated by slip trace analysis in Zn and its alloys. Observed here low activity of the non-basal slip system stands in contrast to the reported 30% contribution of pyramidal $\langle c+a \rangle$ slip to the total deformation of pure Zn with a grain size of 15 μm [16]. However, this may be explained by phenomena observed in magnesium. The grain refinement from 36 μm to 5 μm in pure Mg significantly enhances basal slip activity at the expense of non-basal deformation [19]. Furthermore, solid solution in Mg alloys reduces the non-basal slip systems activity, which operates mainly as a deformation accommodation mechanism regardless of grain size [31]. Similar effects may occur in the investigated here Zn–0.5Cu alloy with a grain size at least five times smaller than reported for pure Zn [16]. Additionally, the low activity of the non-basal slip systems may result from the enhanced degree of freedom for the movement of surface grains, which abolishes von Mises criterion for five independent shear systems omitting the need for activation of high-stress slip systems [32].

The direct effect of strain rate on the slip systems activity results from the GBS activity at various strain rates rather than slip activity itself. According to Eq. 1, lowering the strain rate decreases the stress required for GBS occurrence, leading to the situation when GBS is activated much easier than dislocation slip. Also, grain refinement plays an essential role in the activity of particular deformation modes. According to the well-known Hall–Petch relationship, grain refinement strengthens polycrystalline materials [33]. Following that, a reduction in grain size simultaneously reduces GBS flow stress (power-law) and strengthens grains (Hall–Petch), ultimately

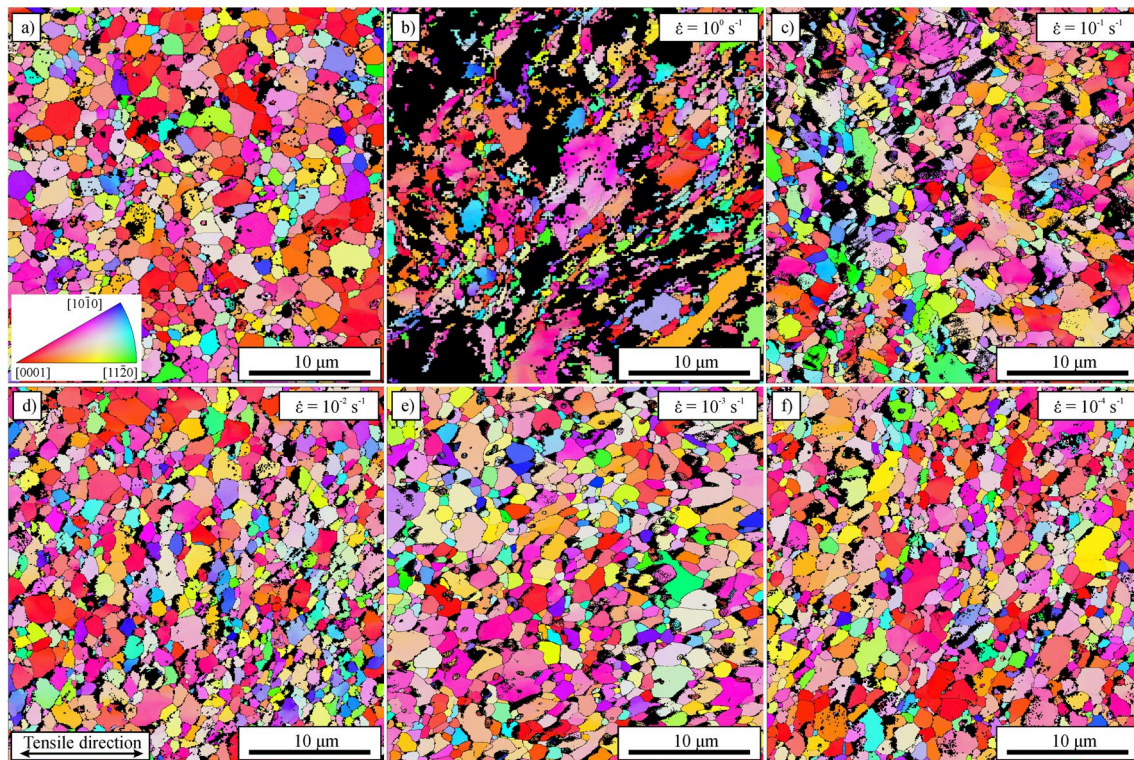


Fig. 9 EBSD maps of **a** undeformed Zn–0.5Cu alloy after ECAP, **b–f** deformed to 25% samples at different strain rates

leading to the activation of GBS at the expense of high-stress slip systems.

Moreover, among possible slip systems in Zn, the basal slip system is activated relatively easily, while the others require significantly higher stress [34]. As already mentioned, the ratio between shear stress in basal, prismatic, and pyramidal $\langle c+a \rangle$ slip systems is usually presented as 1:15:10 [14]. Thus, high plastic anisotropy and GBS are responsible for the observed slip activity changes. As the easiest-to-activate slip system, the basal slip system realizes most of the deformation at high-strain rates, while the prismatic and pyramidal slip systems were activated mostly to accommodate the plastic flow, governed by the basal slip system. At the lower strain rates, GBS shear stress drops below the non-basal slip systems' shear stress; therefore, GBS substitutes the non-basal slip systems as a mechanism allowing uniform deformation by only the basal slip system. Finally, GBS freely realizes a deformation at the lowest strain rate, and the basal slip system operates as a GBS-induced accommodation mechanism.

5 Conclusions

The first combined investigation of GBS and slip systems activity in Zn alloys revealed the significant effect of strain rate on both deformation mechanisms in fine-grained

Zn–0.5Cu alloy. The results presented here for the first time clearly show the complexity of deformation mechanisms in fine-grained Zn–0.5Cu, at radically different strain rate conditions.

- GBS contribution in total deformation ξ changes from 35% at the strain rate 10^0 s^{-1} to 70% at the strain rate 10^{-4} s^{-1} , during tension up to 25% and 50%. The changes reflect the power-law relationship of superplastic behavior and indicate GBS-controlled deformation in the investigated alloy.
- A fraction of grains identified as deformed by slip decreases from 97.5% to 8% for samples strained up to 25% with the reduction in strain rate from 10^0 s^{-1} to 10^{-4} s^{-1} . Basal slip system activity plays a significant part in total dislocation slip deformation. However, rate-controlled basal slip activity suggests its secondary role in the deformation behavior of fine-grained Zn–0.5Cu alloy.
- Only approx. 3% and 7% of grains deformed through non-basal slip systems at strain rates below 10^{-1} s^{-1} and at 10^0 s^{-1} , respectively. Low activity of non-basal slip systems indicates a higher grain refinement strengthening effect on these slip systems than on basal slip.

Acknowledgements This work was supported by the National Science Centre, Poland, Grant number: UMO-2018/31/N/ST8/01062 (WB). JK acknowledges the financial support of the Polish National Science Centre under grant number: UMO-2021/43/D/ST8/03183. The research results presented in this paper have been partly developed with the use of equipment financed from the funds of the "Excellence Initiative—Research University" program at AGH University of Krakow.

Data availability The data presented in this study are available in the repository of the corresponding author.

Declarations

Conflict of interest The authors have no competing interests to declare that are relevant to the content of this article.

Ethical approval This article does not contain any studies with human participants or animals performed by any of the authors.

Open Access This article is licensed under a Creative Commons Attribution 4.0 International License, which permits use, sharing, adaptation, distribution and reproduction in any medium or format, as long as you give appropriate credit to the original author(s) and the source, provide a link to the Creative Commons licence, and indicate if changes were made. The images or other third party material in this article are included in the article's Creative Commons licence, unless indicated otherwise in a credit line to the material. If material is not included in the article's Creative Commons licence and your intended use is not permitted by statutory regulation or exceeds the permitted use, you will need to obtain permission directly from the copyright holder. To view a copy of this licence, visit <http://creativecommons.org/licenses/by/4.0/>.

References

- Kabir H, Munir K, Wen C, Li Y. Recent research and progress of biodegradable zinc alloys and composites for biomedical applications: Biomechanical and biocorrosion perspectives. *Bioact Mater*. 2021;6:836–79. <https://doi.org/10.1016/j.bioactmat.2020.09.013>.
- Q. Liu, A. Li, S. Liu, Q. Fu, Y. Xu, J. Dai, P. Li, S. Xu, Cytotoxicity of Biodegradable Zinc and Its Alloys: A Systematic Review, *J. Funct. Biomater*. 14 (2023). <https://doi.org/10.3390/jfb14040206>.
- M. Wątroba, W. Bednarczyk, J. Kawałko, S. Lech, K. Wiczerzak, T.G. Langdon, P. Bała, A Novel High-Strength Zn-3Ag-0.5Mg Alloy Processed by Hot Extrusion, Cold Rolling, or High-Pressure Torsion, *Metall. Mater. Trans. A*. 51 (2020) 3335–3348. <https://doi.org/10.1007/s11661-020-05797-y>.
- Yang M, Yang L, Peng S, Deng F, Li Y, Yang Y, Shuai C. Laser additive manufacturing of zinc: formation quality, texture, and cell behavior. *Bio-Design Manuf*. 2023;6:103–20. <https://doi.org/10.1007/s42242-022-00216-0>.
- Bednarczyk W, Wątroba M, Kawałko J, Bała P. Can zinc alloys be strengthened by grain refinement? A critical evaluation of the processing of low-alloyed binary zinc alloys using ECAP. *Mater Sci Eng A*. 2019;748:357–66. <https://doi.org/10.1016/j.msea.2019.01.117>.
- Jarzębska A, Maj Ł, Bieda M, Chulist R, Wojtas D, Wątroba M, Janus K, Rogal Ł, Sztwiertnia K. Dynamic Recrystallization and Its Effect on Superior Plasticity of Cold-Rolled Bioabsorbable Zinc-Copper Alloys. *Materials (Basel)*. 2021;14:3483. <https://doi.org/10.3390/ma14133483>.
- Langdon TG. An evaluation of the strain contributed by grain boundary sliding in superplasticity. *Mater Sci Eng A*. 1994;174:225–30. [https://doi.org/10.1016/0921-5093\(94\)91092-8](https://doi.org/10.1016/0921-5093(94)91092-8).
- Mostaed E, Ardakani MS, Sikora-Jasinska M, Drelich JW. Precipitation induced room temperature superplasticity in Zn-Cu alloys. *Mater Lett*. 2019;244:203–6. <https://doi.org/10.1016/j.matlet.2019.02.084>.
- W. Bednarczyk, M. Wątroba, J. Kawałko, P. Bała, Determination of room-temperature superplastic asymmetry and anisotropy of Zn-0.8Ag alloy processed by ECAP, *Mater. Sci. Eng. A*. 759 (2019) 55–58. <https://doi.org/10.1016/j.msea.2019.05.029>.
- Mostaed E, Sikora-Jasinska M, Ardakani MS, Mostaed A, Reaney IM, Goldman J, Drelich JW. Towards revealing key factors in mechanical instability of bioabsorbable Zn-based alloys for intended vascular stenting. *Acta Biomater*. 2020;105:319–35. <https://doi.org/10.1016/j.actbio.2020.01.028>.
- S. Zhu, C. Wu, G. Li, Y. Zheng, J.F. Nie, Microstructure, mechanical properties and creep behaviour of extruded Zn-xLi (x = 0.1, 0.3 and 0.4) alloys for biodegradable vascular stent applications, *Mater. Sci. Eng. A*. 777 (2020) 139082. <https://doi.org/10.1016/j.msea.2020.139082>.
- Langdon TG. Grain boundary sliding revisited: Developments in sliding over four decades. *J Mater Sci*. 2006;41:597–609. <https://doi.org/10.1007/s10853-006-6476-0>.
- Partridge PG. The crystallography and deformation modes of hexagonal close-packed metals. *Metall Rev*. 1967;12:169–94. <https://doi.org/10.1179/mtlr.1967.12.1.169>.
- R. Parisot, S. Forest, A. Pineau, F. Grillon, X. Demonet, J.-M. Maitaigne, Deformation and damage mechanisms of zinc coatings on hot-dip galvanized steel sheets: Part I. Deformation modes, *Metall. Mater. Trans. A*. 35 (2004) 797–811. <https://doi.org/10.1007/s11661-004-0007-x>.
- Cepeda-Jiménez CM, Molina-Aldareguia JM, Pérez-Prado MT. Origin of the twinning to slip transition with grain size refinement, with decreasing strain rate and with increasing temperature in magnesium. *Acta Mater*. 2015;88:232–44. <https://doi.org/10.1016/j.actamat.2015.01.032>.
- Frydrych K, Jarzębska A, Virupakshi S, Kowalczyk-Gajewska K, Bieda M, Chulist R, Skorupska M, Schell N, Sztwiertnia K. Texture-Based Optimization of Crystal Plasticity Parameters: Application to Zinc and Its Alloy. *Metall Mater Trans A*. 2021. <https://doi.org/10.1007/s11661-021-06285-7>.
- Cauvin L, Raghavan B, Bouvier S, Wang X, Meraghni F. Multi-scale investigation of highly anisotropic zinc alloys using crystal plasticity and inverse analysis. *Mater Sci Eng A*. 2018;729:106–18. <https://doi.org/10.1016/j.msea.2018.05.038>.
- B. Fernández Silva, J. Kawałko, K. Muszka, M. Jackson, K. Fox, B.P.P. Wynne, Deformation modes investigation during ex-situ dwell fatigue testing in a bimodal near- α titanium alloy, *Int. J. Fatigue*. 163 (2022) 107098. <https://doi.org/10.1016/j.ijfatigue.2022.107098>.
- Cepeda-Jiménez CM, Molina-Aldareguia JM, Pérez-Prado MT. Effect of grain size on slip activity in pure magnesium polycrystals. *Acta Mater*. 2015;84:443–56. <https://doi.org/10.1016/j.actamat.2014.10.001>.
- W. Bednarczyk, J. Kawałko, M. Wątroba, P. Bała, Achieving room temperature superplasticity in the Zn-0.5Cu alloy processed via equal channel angular pressing, *Mater. Sci. Eng. A*. 723 (2018) 126–133. <https://doi.org/10.1016/j.msea.2018.03.052>.
- Henseler T, Osovski S, Ullmann M, Kawalla R, Pahl U. GTN model-based material parameters of AZ31 magnesium sheet at various temperatures by means of SEM in-situ testing. *Crystals*. 2020;10:1–19. <https://doi.org/10.3390/cryst10100856>.
- Bachmann F, Hielscher R, Schaeßen H. Texture Analysis with MTEX – Free and Open Source Software Toolbox. *Solid State Phenom*. 2010;160:63–8. <https://doi.org/10.4028/www.scientific.net/SSP.160.63>.

23. D. Mainprice, F. Bachmann, R. Hielscher, H. Schaeben, Descriptive tools for the analysis of texture projects with large datasets using MTEX : strength, symmetry and components, Geol. Soc. London, Spec. Publ. 409 (2015) 251–271. <https://doi.org/10.1144/SP409.8>.
24. Mungole T, Kumar P, Kawasaki M, Langdon TG. The contribution of grain boundary sliding in tensile deformation of an ultrafine-grained aluminum alloy having high strength and high ductility. *J Mater Sci*. 2015;50:3549–61. <https://doi.org/10.1007/s10853-015-8915-2>.
25. W. Bednarczyk, J. Kawałko, M. Wątroba, N. Gao, M.J. Starink, P. Bała, T.G. Langdon, Microstructure and mechanical properties of a Zn-0.5Cu alloy processed by high-pressure torsion, *Mater. Sci. Eng. A*. 776 (2020) 139047. <https://doi.org/10.1016/j.msea.2020.139047>.
26. Chokshi AH. An evaluation of the grain-boundary sliding contribution to creep deformation in polycrystalline alumina. *J Mater Sci*. 1990;25:3221–8. <https://doi.org/10.1007/BF00587678>.
27. N. Mollaei, S.M. Fatemi, M.R. Aboutalebi, S.H. Razavi, W. Bednarczyk, Dynamic recrystallization and deformation behavior of an extruded Zn-0.2 Mg biodegradable alloy, *J. Mater. Res. Technol.* 19 (2022) 4969–4985. <https://doi.org/10.1016/j.jmrt.2022.06.159>.
28. Wątroba M, Bednarczyk W, Kawałko J, Bała P. Fine-tuning of mechanical properties in a Zn–Ag–Mg alloy via cold plastic deformation process and post-deformation annealing. *Bioact Mater*. 2021;6:3424–36. <https://doi.org/10.1016/j.bioactmat.2021.03.017>.
29. A. Gokhale, S. R. E.-W.W. Huang, S.Y. Lee, R. Prasad, S.S. Singh, J. Jain, R. Sarvesha, E.-W.W. Huang, S. Yeol Lee, R. Prasad, S.S. Singh, J. Jain, Quantitative evaluation of grain boundary sliding and its dependence on orientation and temperature in pure Zn, *Mater. Lett.* 246 (2019) 24–27. <https://doi.org/10.1016/j.matlet.2019.03.025>.
30. T. Matsunaga, K. Takahashi, T. Kameyama, E. Sato, Relaxation mechanisms at grain boundaries for ambient-temperature creep of h.c.p. metals, *Mater. Sci. Eng. A*. 510–511 (2009) 356–358. <https://doi.org/10.1016/j.msea.2008.06.055>.
31. Shi DFF, Pérez-Prado MTT, Cepeda-Jiménez CMM. Effect of solutes on strength and ductility of Mg alloys. *Acta Mater*. 2019;180:218–30. <https://doi.org/10.1016/j.actamat.2019.09.018>.
32. Sheikh-Ali AD, Garmestani H. Evolution of surface and bulk textures during superplastic deformation in a zinc alloy. *Mater Lett*. 2007;61:478–81. <https://doi.org/10.1016/j.matlet.2006.04.093>.
33. Hall EO. The Deformation and Ageing of Mild Steel: III Discussion of Results. *Proc Phys Soc Sect B*. 1951;64:747–53. <https://doi.org/10.1088/0370-1301/64/9/303>.
34. Bednarczyk W, Wątroba M, Jain M, Mech K, Bazarnik P, Bała P, Michler J, Wiecek K. Determination of critical resolved shear stresses associated with <a> slips in pure Zn and Zn-Ag alloys via micro-pillar compression. *Mater Des*. 2023;229: 111897. <https://doi.org/10.1016/j.matdes.2023.111897>.

Publisher's Note Springer Nature remains neutral with regard to jurisdictional claims in published maps and institutional affiliations.